ACS APPLIED MATERIALS & INTERFACES

www.acsami.org

Research Article

Snap-through in Graphene Nanochannels: With Application to Fluidic Control

Shuping Jiao and Mingchao Liu*

Cite This: *ACS Appl. Mater. Interfaces* 2021, 13, 1158–1168

Read Online

ACCESS | Metrics & More | Article Recommendations | Supporting Information

ABSTRACT: Recent studies on the structure and transport behaviors of water confined within lamellar graphene have attracted intense interest in filtration technology, but the mechanism of water transport in complex membrane nanostructures remains an open question. For example, similar systems but at much larger scales have indicated that the instabilities of an elastic structure, such as snap-through, play an essential role in controlling the fluid flow. Graphene sheets, which have an atomic thickness, often appear highly wrinkled in nanofluidic devices and so are vulnerable to elastic instabilities. However, it remains unclear how does the flexible wrinkled structure affect the transport of water and filtration efficiency or whether such an effect can be exploited in devices. In this work, we explore the flow-induced snap-through in graphene nanochannels by combining molecular simulations with the theoretical analysis. We further demonstrate its applications to passive control of fluid flow and to ion/molecule selection. By introducing a flexible arch embedded within a graphene nanochannel, we observe the "snap" of the arched graphene wall from one stable state to another by varying the fluid flux (i.e., velocity); the critical velocity of this snap transition is found to depend nonmonotonically on the geometric size of the channel and the arch. We also demonstrate reversible snap-through by fixing the end parts of the flexible arch. These results suggest the potential of flow-induced snap-through in graphene-based nanochannels for ion/molecule selection applications in, for example, the design of a foul-resistant, easy-to-clean, reusable filter membrane.

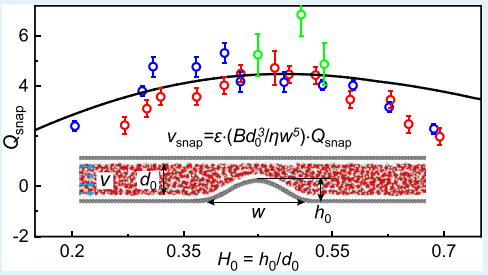

KEYWORDS: *graphene nanochannel, flexible wrinkles, snap-through, fluidic control, molecule selection*

INTRODUCTION

Controlled transport and selection of molecules and ions through membranes are important in applications as diverse as water purification and ion separation.[1,2] Extending the low-dimensional fluidic technologies to the nanoscale led to unexpected water- and ion-structures and transport phenomena.[3,4] In recent studies, laminates of graphene (or graphene oxide, GO) were highly promising for excellent separation membrane of gas and liquid molecules due to their high permeability, tunable selectivity, and ultralow thickness.[5−11] In the separation process, it is generally believed that the molecules and ions penetrate the membrane through nanopores and/or nanochannels in the graphene laminate. For the dry membrane, the channel gap is too narrow to permit even the passage of helium.[12] However, due to the presence of oxidation groups on the graphene layer, the laminate can swell in aqueous surroundings, allowing for the transport of water and small ions/molecules.[13,14] Limited by the channel size, large ions are normally blocked. The size of the blocked ions can be selected by tuning the interlayer spacing of the laminates.[1,2] Benefiting from these advantages, graphene laminates are widely pursued for cost-effective water treatment technologies, such as purification, filtration, and desalination.

Water permeation and ion separation through graphene nanochannels, carbon nanotubes (CNTs), and CNT porins were reported recently, with observed permeability higher than the prediction from the no-slip viscous flow.[12,15−17] This enhancement was attributed to the slippery nature of water flow through pristine graphene and the capillary pressure acting as an additional driving force for the flow.[12,16−18] Moreover, the separation capability usually originates from the size effect of nanochannels. Despite the technological interest in graphene laminates, a clear understanding of the factors that dictate water transport within the layers has not yet emerged because of the complex microstructure involved, such as modified functional groups, pores, ripples, wrinkles, folds, and noncompact stacking.[19,20] To elucidate the underlying mechanism of the high permeability of water within complex and circuitous pathways through laminates,[12,21] it has been surmised that interconnected, graphene-based nanochannels within GO and ordered water structure exist in the laminates.[22−25] The pinholes, wrinkles, and imperfect sheet packing are also considered to play important roles in the

Received: September 12, 2020
Accepted: December 10, 2020
Published: December 23, 2020

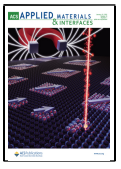

https://dx.doi.org/10.1021/acsami.0c16468
ACS Appl. Mater. Interfaces 2021, 13, 1158−1168

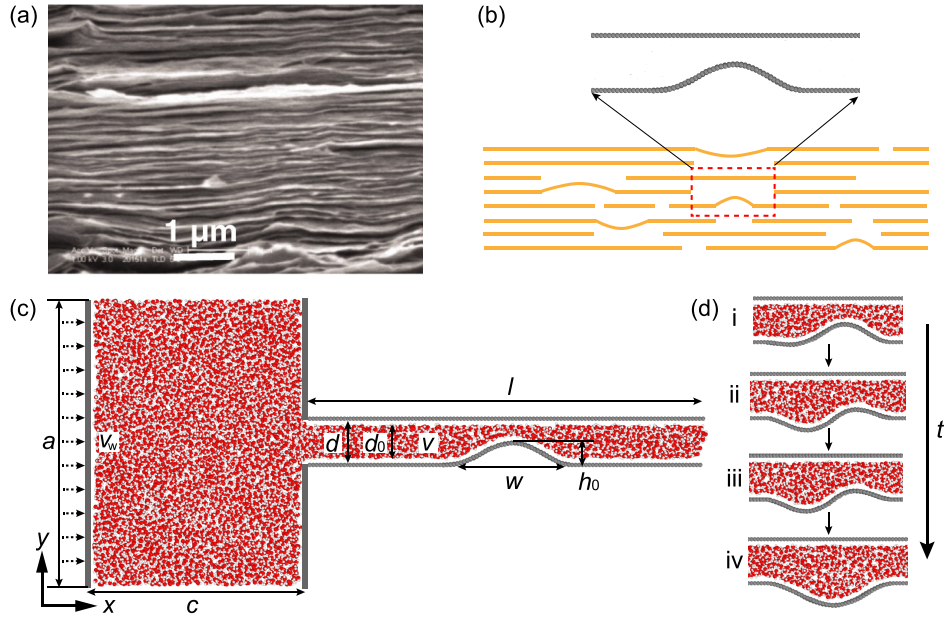

Figure 1. (a) Electron micrograph of the graphene film's cross section. Reproduced with permission from ref 12. Copyright 2012 American Association for the Advancement of Science. (b) Schematic view for a possible water permeation path in graphene laminates with nanochannels. (c) Molecular structures of MD simulation consisting of a graphene nanochannel connected to a reservoir (of width and length a = 10.1 nm and c = 8.0 nm, respectively); the length and width of the graphene nanochannel are l = 14.8 nm and d = 1.65 nm (d_0 = 1.31 nm), respectively, while the depth in the z direction is e = 2.1 nm; $w = w_0$ = 4.57 nm is the span of the arch and h_0 = 0.33−0.94 nm is the amplitude of the arch corresponding to the initial undeformed configuration. (d) Dynamic snapshots of the configuration evolution of the flexible arch during the snapping process.

molecular transport and separation depending on the sheet size and assembly process.[5,6,19,21,26]

The filtration effects of parallel stacked nanochannels, nanoslits, and nanopores have been widely explored. However, in most of the previous studies, nanochannels in graphene laminates are modeled as nondeformable walls regardless of their flexibility and fluid−solid coupling effect in the flux.[3,12,18,27,28] Due to the extremely low out-of-plane stiffness of graphene sheets, uneven structures, such as ripples, wrinkles, and crumples, are plentiful in the stacked graphene membrane.[19,29] Besides, the wrinkled wall can be deformed under pressure during the liquid flow process, and in turn, the deformation of the wall affects the liquid flow process, as well as the function of the membrane (i.e., molecule selection). Therefore, the influences of membrane flexibility and wrinkled structures on liquid transport and filtration efficiency, as well as the regulating effect of fluid flow on flexible wrinkled structures, need further investigation. This constitutes the main motivation of this work; we focus on the influence of flexible wrinkled structures on membrane transport and filtration efficiency.

From a macroscopic point of view, recent studies have indicated that a flexible material can be adopted to control the fluid (including both gas and liquid) flow in fluidic devices.[30−33] In this kind of flexible fluidic device, the fluid flow and the wall deformation are coupled to each other. Comparing with the rigid fluidic device, the flexible wall plays an important role in solid−fluid coupling behaviors, which might further be harnessed for the control of the fluid flow process. More interestingly, the snap-through instability, which has been adopted in biology and engineering to generate fast motions between two states, has shown potential for the passive control of viscous flow.[31] By embedding an elastic arch into a flow channel, the arch can snap between constricting and unconstricting states thereby changing the fluid flux. Benefiting from the solid−fluid coupling feature, the flow process can also be self-regulated when the state of the arch is snapped. This novel device showed a good demonstration for the design of passive fluidic devices. In the meantime, this macroscopic design principle also inspires us to harness the snap-through instability to control the micro/nanoscale fluid flow.

In this work, we explore the flow of water and its induced snap-through behavior in graphene membranes with wrinkles by performing molecular dynamics (MD) simulations, in which the wrinkled graphene membrane is modeled as a nanochannel with a flexible arch. We observe the snap-through transition of the arched structure when water flows through the nanochannel with a flow rate greater than a critical value. Nonmonotonic dependence of this critical snap-through velocity on the arch size is obtained, which can be predicted by a theoretical model that combines the beam model and the lubrication theory. We further calculate the evolution of the structure of the arched graphene and the hydrodynamic pressure during the flow process. We also design a graphene nanochannel with reversible snap-through feature controlled by flow, which offers a guide for the design of recyclable, clog-proof nanofiltration membranes with both high permeability and selectivity. As a demonstration, we finally discuss the feasibility and efficiency of ion/molecule selection using this snap-through-based graphene nanochannel.

RESULTS

Molecular Structures and Water Flow-Induced Snap-through in Graphene Nanochannels. To model the flow of water through lamellar graphene with multiple wrinkles of different sizes as shown in Figure 1a,b, we simplify the structure as a graphene nanochannel with two parallel rigid graphene sheets (see Figure 1c). The sheet on the top is fully

https://dx.doi.org/10.1021/acsami.0c16468
ACS Appl. Mater. Interfaces 2021, 13, 1158−1168

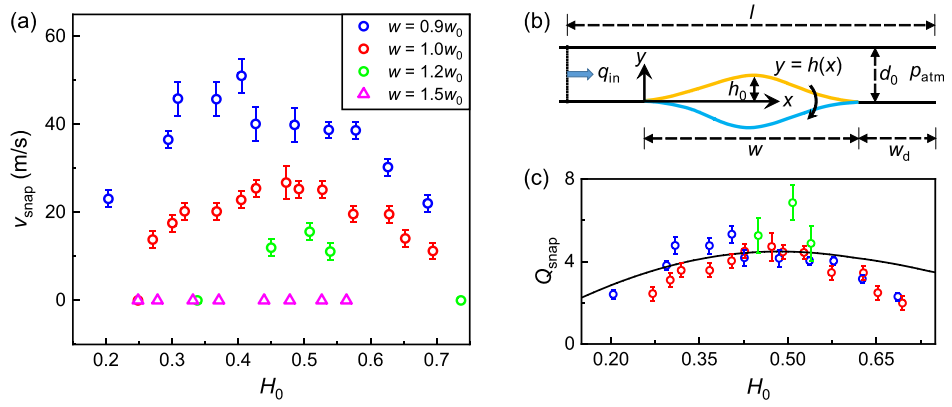

Figure 2. (a) Dependence of the critical velocity of snap-through, v_{snap}, calculated from simulation on the channel blocking parameter, $H_0 = h_0/d_0$, where h_0 is the amplitude of the arch and d_0 and w are the effective width of the channel and the span of the arch, respectively (here, we fix d_0 = 1.31 nm). The data for different cases with different arch spans ($w \in \{0.9, 1.0, 1.2, 1.5\}\cdot w_0$, with w_0 = 4.57 nm) are shown by different symbols with different colors, and error bars represent the uncertainty corresponding to the upper and lower bounds of the critical velocity measured in simulation. (b) Schematic diagram of the bistable nanochannel involving an arch arranged next to a lubrication-type flow. (c) Dimensionless flux Q_{snap} (rescaled according to eq 6) versus the channel blocking parameter H_0 for the cases with finite v_{snap} (i.e., $w = 0.9w_0$, $1.0w_0$, $1.2w_0$); the data collapse onto the prediction of our theoretical model (solid black curve).

rigid, and the bottom one is composed of two rigid parts on both sides and a flexible arch (of span w and amplitude h_0) embedded in the middle. The flexible arch can deform when the fluid flows in the channel. It is noted that the amplitude h_0 corresponds to the initial undeformed configuration of the arch. The graphene nanochannel (length l, width d, and depth e) and the connected reservoir (length c, width a, and depth e) are filled with water molecules (the depth is perpendicular to the xOy plane and is not displayed in this figure). Here, it should be noted that d is measured as the distance between two carbon planes and the effective width of the channel should be considered to be $d_0 = d - d'$, which we refer to as the effective interlayer spacing,[2] where d' = 0.34 nm is the van der Waals interaction radius of graphene sheets.[34] To make water molecules flow in the channel, they are accelerated through the action of a uniformly accelerating piston at the end of the water reservoir; the velocity v_w of this piston is converted to an entrance velocity v in the channel through the incompressibility of the liquid according to $v = (a/d_0)\cdot v_w$ (Figure 1c). To avoid the deformation of the arch structure during flow acceleration, the arch is first constrained inward by fixing a bunch of carbon atoms at the middle of the arch until a uniform velocity is reached in the channel (as shown in Figure S1, the number of water molecules flowing out of the outlet reaches the expected linear dependence on time after about 0.3 ns). We then release the constraint on the middle part of the arch so that it restores to the completely flexible state and, therefore, to allow for the flexible arch to deform in the stable flow. Snap-through of the arch occurs when the flow velocity exceeds a critical value; snapshots of the arch configuration are shown in Figure 1d and Movie S1. As the flow velocity increases, the shape of the flexible arch changes slightly at first (Figure 1d-i), similar to the initial shape, and then develops to an asymmetric "s" shape (Figure 1d-ii,iii), before finally snapping to the opposite side (Figure 1d-iv).

According to the simulation, snap-through of the arch occurs when the flow velocity exceeds a critical value. To quantify this critical velocity of snap-through, v_{snap}, we perform a series of simulations with different arch amplitudes, h_0, and spans, w (fixing d_0 = 1.31 nm; see Figure 1c). For each arch of specified amplitude h_0 and span w, the critical velocities are determined from a series of constant flow simulations with different velocities; determining the minimum velocity at which snap-through occurs and the maximum velocity at which snap-through does not occur allows for an interval for v_{snap}. Here, it should be noted that the low friction between graphene and water causes flow slippage in the nanochannel, thereby enhancing the flow.[22] Given the nonuniform velocity profile across the y-direction within the channel, we calculate the average value to identify the critical velocity. For the arch with span $w = w_0$ = 4.57 nm, the dependence of the critical velocity v_{snap} on the channel blocking parameter H_0, where $H_0 = h_0/d_0$ is the ratio of the arch amplitude h_0 and the effective channel width d_0, which characterizes the extent of the blocking of the channel by the arch, is shown in Figure 2a by red circles. The error bars indicate the measurement uncertainty in the critical velocity (the upper and lower bounds of the critical velocity measured in simulations). It is interesting to find that the value of v_{snap} is a nonmonotonic function (first increases and then decreases) of the blocking parameter H_0. If H_0 is small enough (i.e., $H_0 \le 0.25$), snap-through can occur even at a near-zero flow velocity, which means that the flexible arch is unstable to thermal fluctuations because of its low deformation energy. When H_0 is large enough (i.e., $H_0 \ge 0.75$, which corresponds to $h_0 \ge 1.0$ nm), the narrowest channel size $d_0 - h_0$ = 0.31 nm is equivalent to the finite size of a water monolayer (~0.31 nm), and so the channel can be considered to be nearly blocked. In this condition, snap-through of the arch occurs at a very low flow velocity because of the large pressure generated by the fluid flow in the nearly blocked channel.

To investigate the effect of the span, w, on snap-through of the arch, except for the case of $w = w_0$ = 4.57 nm, we perform a series of simulations with different spans, $w \in \{0.9, 1.2, 1.5\}\cdot w_0$. It is found that the critical velocity is very sensitive to the value of w. For the flattest arch (i.e., $w = 1.5w_0$), simulations show that the arch always deforms outward spontaneously for different H_0 values even with zero flow velocities (pink upper triangles in Figure 2a). This indicates that when the size of the arch is large enough, its bending stiffness is not enough to resist thermal fluctuations due to the flexible nature of graphene and there is no snap-through transition. For $w = 1.2w_0$, since the bending stiffness is a bit larger than the flattest

https://dx.doi.org/10.1021/acsami.0c16468
ACS Appl. Mater. Interfaces 2021, 13, 1158−1168

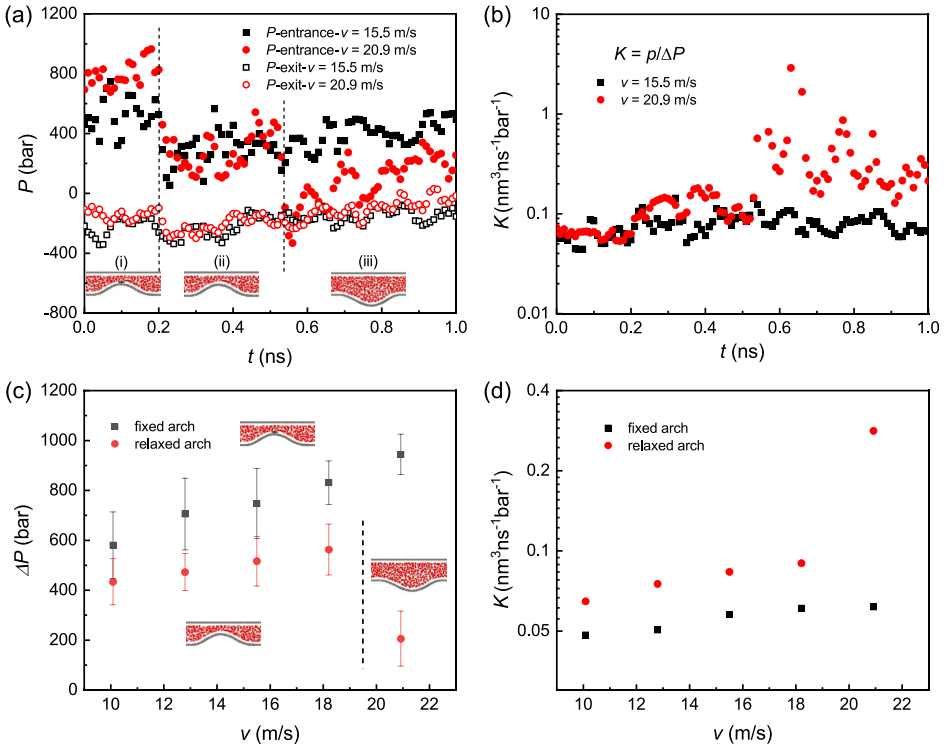

Figure 3. (a) Evolution of the hydrodynamic pressure at the entrance (filled symbols) and exit (empty symbols) of the channel with flow velocities of v = 15.5 m/s (squares) and v = 20.9 m/s (circles) during the snap-through process in the channel with geometric sizes w = 4.57 nm and H_0 = 0.63. (b) Evolution of the effective hydraulic conductivity K with flow velocities of v = 15.5 m/s (black squares) and v = 20.9 m/s (red circles). (c) Pressure difference between the entrance and the exit, ΔP, and (d) hydraulic conductivity, K, at the steady state (corresponding to the final state in Figure 3a,b) is plotted as a function of flow velocity, v, in the channels with unconstrained (black squares) and constrained arched structures (red circles).

case, the nonmonotonic dependence of v_{snap} over H_0 can be found in a narrow range of H_0, say $0.4 < H_0 < 0.6$, as shown by green circles in Figure 2a. With $w = 0.9w_0$, corresponding to a sharper arch (compared with the case of $w = w_0$), for each specific H_0, the arch is more stable and the critical velocity is higher than the corresponding case of $w = w_0$ (see blue circles in Figure 2a). Particularly, the nonmonotonic relation between v_{snap} and H_0 still holds, even in a broader range ($0.2 < H_0 < 0.75$). Based on the above results, we see that snap-through occurs within a certain geometric size range, and this quantitative information is helpful for the design of nanofluidic devices.

The nonmonotonic relation between v_{snap} and H_0 can be attributed to the nonlinear coupling between the fluid flow in the channel and the elastic deformation of the flexible arch. The basic mechanism of snap-through of the arch is the flow-generated pressure applied to the arch to push the midpoint away from its original position, and snap-through occurs as soon as the midpoint is pushed downward (by an amount of pressure) comparable to its initial amplitude h_0 (the pressure just exceeds the threshold at this point), which can be analogous to point indentation.[35] Since we controlled the flow velocity (or flux) in the channel entrance, the pressure scales as $p \propto v/(d_0 - h_0)^3 (\propto v/(1 - H_0)^3)$ according to Poiseuille's law. Pressure-induced deformation is expected to linearly increase with pressure p. As we mentioned above, the threshold condition of snap-through is that the deformation induced by the critical pressure p_{snap} is comparable to the channel amplitude. We can expect that for a small channel blocking parameter, $H_0 \ll 1$, the critical snap-through velocity v_{snap} linearly increases as h_0 (i.e., H_0) increases. However, when the arch amplitude h_0 becomes comparable to the channel width d_0 (i.e., the blocking parameter is relatively large, namely, $H_0 \sim 1$), the increase of critical pressure p_{snap} as H_0 increases is dominated by the term $1/(1 - H_0)^3$, and v_{snap} decreases accordingly. It is clearly seen that these scaling arguments agree with the nonmonotonic trend of v_{snap} to H_0 in Figure 2a qualitatively.

To quantitatively model the coupling of the fluid flow and the arch's deformation involved in the flow-induced snap-through of the graphene nanochannel, we simplify the simulation system (i.e., Figure 1c) as a two-dimensional (2D) physical model, as shown in Figure 2b, in which the flexible arch can snap from the original state (the upper yellow curve) to the inverted state (the lower blue curve) under the pressure load during the fluid flow process. This coupling system can be described by adopting the linear beam model and the lubrication theory (see the Models and Methods section for details). According to the analysis, the critical velocities, v_{snap}, for different cases with different arch spans, w, can be rescaled to the critical nondimensional flux Q_{snap} through eq 6. It can be seen that all of the simulation data (the dependence of Q_{snap} on H_0) for three cases ($w = 0.9w_0$, $1.0w_0$, $1.2w_0$) mainly collapse onto a master curve (see Figure 2c). The main trend of the collapsed simulation data, i.e., the nonmonotonic dependence of Q_{snap} on H_0 with the maximum value of Q_{snap} appearing at $H_0 \approx 0.5$, can be quantitatively predicted by the theoretical model, eqs 1−6, as shown by the solid black curve. However, the value of Q_{snap} is overestimated for both small and large H_0 values, an effect that may be

https://dx.doi.org/10.1021/acsami.0c16468
ACS Appl. Mater. Interfaces 2021, 13, 1158−1168

attributed to the inaccuracy of the linear elastic beam theory for describing the deformation of the graphene arch. For example, here we used a constant bending stiffness of the graphene layer while the stiffness is known to increase slightly with increasing the applied curvature.[36] At the same time, thermal fluctuations, which are inevitable at such small length scales, could cause significant enhancement of the bending stiffness of the sheet.[37] Another factor is that we neglected the slip effect of the water flow in the lubrication theory. It is known that the slip flow induces significant flow rate enhancement[18] and changes the pressure distribution accordingly. To quantify the complex slip effect in nonuniform nanochannels is quite challenging. Here, we only simply introduced the constant enhancement factor (ε, see eq 6 in the Theoretical Model Analysis section for details) to modify the theoretical model, which introduces inaccuracy in the obtained results. In addition, considering that the channel size is sufficiently small, especially for the case with a large blocking parameter H_0 (which corresponds to small channel size $d_0 - h_0$), the flow of water molecules may behave as a subcontinuum transport.[38] This subcontinuum transport cannot be precisely described by the lubrication theory that we adopted, which is on the basis of continuous flow, and may mainly result in the deviation of our prediction for large H_0 (the right bound in Figure 2c).

To characterize the snap-through behavior of the flexible arch, we also measure the pressure at the entrance (upstream) and exit (downstream) of the channel in the simulations during the snapping process. The results of two cases with velocities of v = 20.9 and 15.5 m/s (w = 4.57 nm and H_0 = 0.63) are shown in Figure 3a by squares and circles, respectively, in which the filled symbols represent the pressure at the entrance and the empty symbols refer to the pressure at the exit. The pressure is reported as the isotropic part of the stress tensor, i.e., $(P_{xx} + P_{yy} + P_{zz})/3$. It should also be noted that the values of the flow velocities and pressures obtained through our simulation are quite larger than the values measured in experiments (the fastest flow velocity reported experimentally in graphene nanochannels is about 1 m/s).[3] These high velocities obtained in MD simulation could be attributed to several factors. One of the main issues is the computational limitation and, more specifically, in the nonequilibrium MD simulations, we normally have to apply a high pressure gradient to obtain the statistically significant and credible velocity field excluding the thermal fluctuation.[39] From this perspective, such large flow velocities and pressure gradients are standard for nonequilibrium MD simulation.[3,18,39] Another possible reason is that the simulation system is entirely ideal, in which the surfaces of graphene layers are completely smooth at the atomic scale and the slip effect is much larger than that in the real experimental system. The synthesized graphene layers in experiments usually contain some additional functional groups and defects, as well as impurities, on their surface, which may weaken the slip effect and therefore significantly reduce the flow velocity under the same pressure gradient.[28,40]

The results of the full simulation process can generally be divided into three stages (see Figure 3a). In stage I (i.e., t < 0.2 ns), the flexible arch is constrained inward; in this stage, the pressure at the entrance remains almost constant even with different flow velocities. In stage II (0.2 ns < t < 0.52 ns), the constraint on the arch is removed and the arch begins to deform slightly but remains deflected inward. An obvious drop of the entrance pressure can be found compared to stage I because the deformation of the arch in the flow changes the effective width of the channel and promotes the flow. One point that should be mentioned is that from stage I to stage II, an unstable process of the flow is experienced due to deformation of the arch coupling with the fluid flow. The evolution of entrance pressure is slightly different for two cases with different velocities. For the case of v = 15.5 m/s, the entrance pressure tends to be a constant except for the large reduction at the beginning, which can be attributed to the large deformation of the arch induced by the inertia effect of the flow, while the entrance pressure for the case of v = 20.9 m/s tends to increase after the initial drop, since the higher pressure generated by the higher velocity (comparing to the case of v = 15.5 m/s) leads to greater deformation of the arch, and snap-through is excited by the higher pressure found at the end of stage II. Finally, stage III (t > 0.52 ns) occurs for the case of v = 20.9 m/s, in which the arch snaps outward accompanied by a sharp drop of the entrance pressure. (Stage III is not observed for the case of v = 15.5 m/s since the arch remains deflected inward with essentially constant entrance pressure after stage I.) It is clearly seen that the change of the entrance pressure is highly relevant to the evolution of the arch shape. Comparing with the entrance pressure, the pressure at the exit is stable during the full process, both before and after snap-through (i.e., in all three stages).

Additionally, the hydraulic conductivities (with the definition of $K = q/\Delta P$, where q is the flow rate, i.e., the fluid volume passing through the channel section per unit time, and ΔP is the pressure difference between the entrance and the exit) are calculated and plotted in Figure 3b. The hydraulic conductivity K measures the ability of the channel to transmit fluid in the presence of an applied pressure gradient, and it is inverse to the flow resistance, $R = \Delta P/q$. It is shown that the value of K remains constant at stage I and is roughly the same for both the cases (v = 15.5 and 20.9 m/s). During the transition from stage I to II, since the constraint at the middle of the arch is suddenly removed, the arch is deformed by the fluid pressure, and then a slight increase of K (which indicates the promotion of flow due to the increase in the narrowest channel width) is found at the beginning of stage II. For the lower-velocity case (v = 15.5 m/s, without snap-through), K remains approximately constant throughout stage II but increases sharply when snap-through occurs at stage III in the higher-velocity case (v = 20.9 m/s). It is worthwhile to note that, as we fixed the middle of the arch in the channel at stage I, it can be regarded as a rigid nanochannel since the deformation of the arch is restricted. After entering stage II, the constraint at the middle of the arch is removed and the channel becomes deformable. These significant changes in the flow field (both ΔP and K) between stages I and II indicate that compared to the rigid nanochannel, the nanochannel with a deformable arch can accelerate the fluid flow.

Furthermore, we calculate the pressure difference ΔP between the entrance and the exit at the steady state with different velocities, which corresponds to the final state in Figure 3a,b, in channels with constrained or unconstrained arches. The result of ΔP is plotted as a function of the flow velocity, v, in Figure 3c. As expected, at a low Reynolds number, a linear dependence of ΔP on v is found in the constrained arched channel (black squares) because the constrained arch in the channel is not allowed to deform during the fluid flow and the channel geometry is independent

https://dx.doi.org/10.1021/acsami.0c16468
ACS Appl. Mater. Interfaces 2021, 13, 1158−1168

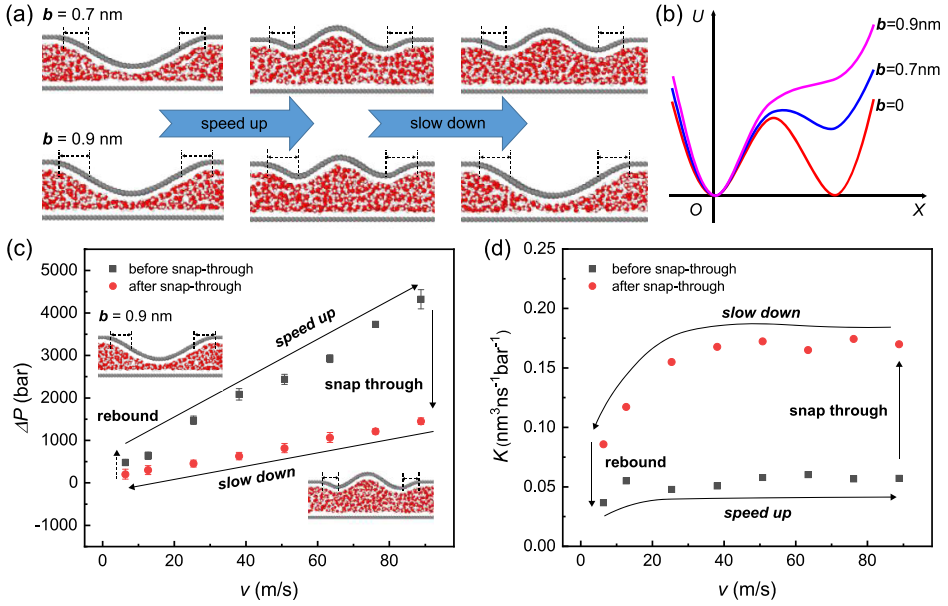

Figure 4. (a) Snapshots of snap-through and the recovery of an arched nanochannel with partially fixed edges for the cases with w = 4.57 nm, H_0 = 0.667, and b = 0.7 nm (top) and 0.9 nm (bottom). (b) Schematic diagram of the energy landscape of the partially fixed arch structures. (c) Pressure difference ΔP and (d) hydraulic conductivity K vary with flow velocity, v, during the speeding up and slowing down processes in the monostable graphene nanochannel with a partially fixed arch (fixed length b = 0.9 nm).

of the flow velocity. For the case of the unconstrained arched channel (red circles), the pressure difference ΔP increases almost linearly with the flow velocity v when the velocity is below the critical snapping value, v_{snap} (left-hand side of the vertical dashed line). Above v_{snap}, we find a sudden drop in the pressure (right-hand side of the vertical dashed line). In the linear (unsnapped) regime, the unconstrained arch remains inward while being deformed slightly, which is also reflected in the slope of ΔP with v being smaller than the constrained arched case. The sudden drop of ΔP at a high flow velocity indicates that snap-through occurs, and the flow resistance is significantly reduced. The hydraulic conductivity $K = q/\Delta P$ at different velocities is also plotted in Figure 3d, in which we find that K remains almost constant unless snap-through of the unconstrained arch has occurred (at a high velocity). In this case, snap-through causes the K of the channel to rise sharply (by a factor of about 4).

Reversible Snap-through of Graphene Nanochannels. The systems we have presented so far are irreversible: the flexible arch does not return to its original state spontaneously after snap-through. This feature may limit its application, e.g., for the ion separation discussed later. To overcome this limitation, we design a reversible snap-through structure by clamping both ends of the flexible arch at a prescribed angle to the horizontal direction, as shown in Figure 4a. More specifically, here, we partially fix both edges of the flexible arch with a finite horizontal projection length b, and the partially fixed arch can be turned from bistable to monostable by changing the fixed length (Figure 4b). In the graphene laminates, a similar boundary constraint may be derived from the irregular assembly and the limit of neighboring graphene sheets. It can be seen from Figure 4a that snap-through of the flexible part of the arch occurs when the flow velocity is higher than a critical value. With decreasing velocity, the snapped part recovers spontaneously for the arch with a larger fixed length (i.e., b = 0.9 nm, as shown in the bottom of Figure 4a), and arch with a smaller fixed length (b = 0.7 nm, the top of Figure 4a) remains in the snapped state. These features can be classified as bistability and monostability for the cases of b = 0.7 and 0.9 nm, respectively, and are also illustrated by the energy landscape of the partially fixed arched structures, as shown in Figure 4b.

In Figure 4b, we presented a schematic diagram of the energy landscape, with x-axis as the middle point displacement and y-axis as the strain energy, for partially fixed arch structures. For arch that is fully flexible or with a minor fixed length, e.g., b = 0, there two potential wells (i.e., local minimum energy states) corresponding to the two stable states (the original one and the inverted one); see the red curve in Figure 4b. In this case, because of the existence of a large energy barrier, the flexible arch cannot return to its original state spontaneously once it snaps to the inverted state, as we have discussed in Figures 1 and 3. On increasing the fixed length of the edge, e.g., b = 0.7 nm, the second potential well that corresponds to the inverted state increases accordingly (which implies that the energy barrier decreases; see the blue curve in Figure 4b). In this case, as shown in the top of Figure 4a, the snapped flexible part of the arch cannot return to its original state spontaneously yet. When the fixed length of the edge is larger than a critical value (which is related to geometrical parameters of both the channel and the arch), e.g., b = 0.9 nm, the inverted state-associated potential well disappears (the pink curve in Figure 4b). In this case, the snapped configuration is not stable; it spontaneously snaps back to the original state as the flow velocity decreases (see the bottom of Figure 4a). We can therefore refer to this as reversible snap-through. This type of arched channel that can perform reversible snap-through provides a design strategy for filters with capabilities of adjustable selectivity and serviceable range, and it makes the channel highly promising for the design of flow sensors and nonblocking and reusable nanofiltration structures. It is worth mentioning that although it might be possible to find some channel-like structures in the experimental synthetic multilayer graphene film with similar

https://dx.doi.org/10.1021/acsami.0c16468
ACS Appl. Mater. Interfaces 2021, 13, 1158−1168

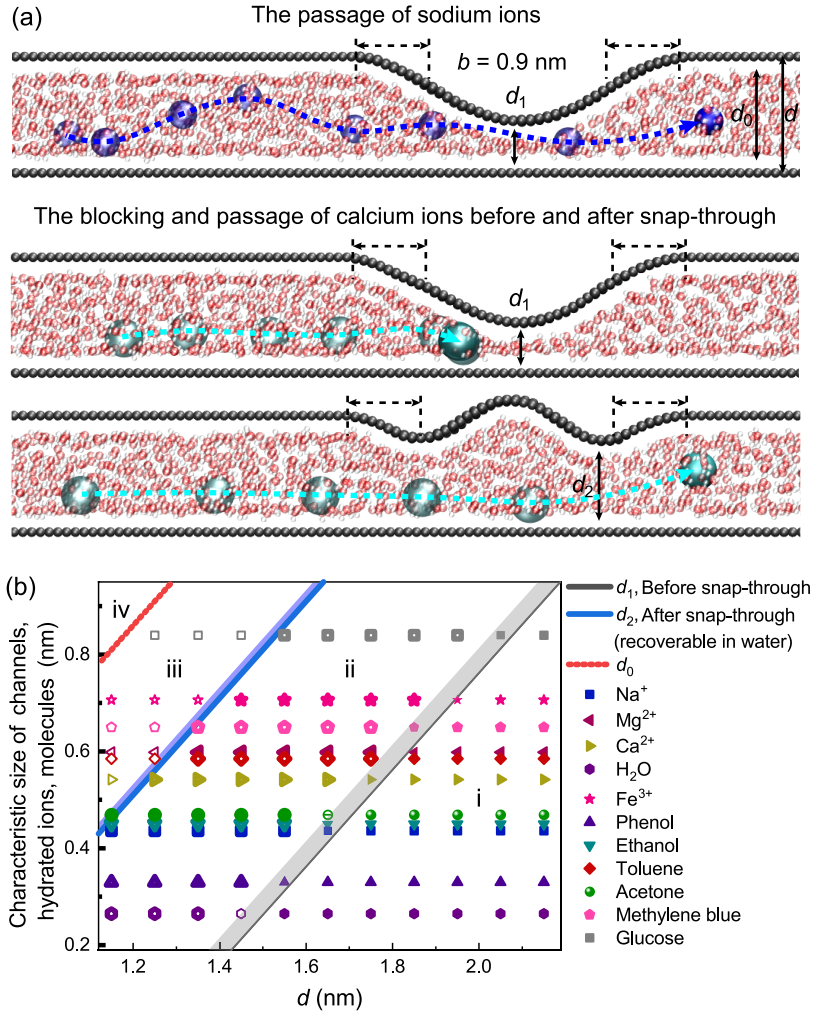

Figure 5. (a) Snapshots of the blockage and passage of ions (Na^+, the top panel, and Ca^{2+}, the bottom two panels) through the arched nanochannel, with characteristic dimensions of w = 4.57 nm, H_0 = 0.667, b = 0.9 nm (for the arch) and d = 1.65 nm (d_0 = 1.31 nm), d_1 = 0.43 nm, d_2 = 0.96 nm (for the channel) before and after snap-through and (b) phase diagram of the selectivity of ions/molecules in the partially fixed arched graphene nanochannels with reversible snap-through in the parameter space (channel width, d, and characteristic size of ions/molecules); the whole space is divided into four phases by the characteristic sizes of the arched channels, d_1, d_2, and d_0. The shaded regions of d_1 and d_2 represent the disturbance of the channel sizes in the flow field. The size of hydrated ions and molecules are taken from ref 43.

characteristics as our model system, it is still challenging to quantitatively fabricate such a device, owing to the limitation of the current experimental techniques. One possible construction strategy that we can expect is to directly synthesize graphene films on carefully designed substrates.

For the purpose of characterization of snap-through behavior of the monostable graphene nanochannel (i.e., b = 0.9 nm), we calculate the pressure difference between the entrance and the exit, ΔP, and the hydraulic conductivity, $K = q/\Delta P$, during the speeding up and slowing down processes, as shown in Figure 4c,d, respectively. The pressure at both the entrance and the exit is measured when the flexible part of the arch stabilized in a steady flow. It can be seen from Figure 4c that the pressure difference ΔP increases as the flow speeds up and then drops suddenly when snap-through occurs (which corresponds to the critical velocity of $v \approx 88.8$ m/s). Then, as the flow slows down (i.e., v decreases), ΔP decreases until the structure spontaneously snaps back to its initial state at $v \approx 6.3$ m/s. Figure 4d shows that the hydraulic conductivity K slightly increases first and then remains constant with further increase in the flow velocity during the speeding-up process. This sharp change in the size of the channel causes a sudden rise of K (by a factor of 3) when snap-through occurs. During the slowing down process, K remains constant first and then gradually decreases. This decrease corresponds to the recovery of the snapped flexible part of the arch as the flow velocity decreases.

It can also be seen from Figure 4c,d that the critical velocity of snap-through for the partially fixed arch is greatly increased compared to that of the fully flexible arched structure. For the case of b = 0.9 nm, the critical velocity (~88.8 m/s) is about 5 times higher than that of the case of the fully flexible arch (b = 0, as discussed in Figure 3). This indicates that the stability of the flexible arch under the fluid flow is enhanced by the introduction of the partially fixed edges. Furthermore, the effects of the fixed length b on the stability of the partially fixed arch structure are also investigated. It is found that the critical velocity of snap-through increases with b and snap-through is not reversible even as the flow velocity decreases to zero for the case of $b < 0.9$ nm while it is spontaneously reversible for the case of $b \geq 0.9$ nm. For comparison, the arched channel of the same size without water filling is also studied, and snap-through is found to not be reversible for $b < 0.7$ nm and

https://dx.doi.org/10.1021/acsami.0c16468
ACS Appl. Mater. Interfaces 2021, 13, 1158−1168

reversible for $b \geq 0.7$ nm. The larger critical value of b for the water-filled channel compared to that of the empty channel may be attributed to the damping from the surrounding water as the arch deforms.

DISCUSSION

Selectivity of Ions in Graphene Nanochannels with Reversible Snap-through. Recently, ultrafast mass transport of liquid and the selection of ions through the GO laminar membrane have been widely reported.[1,2,12,41,42] However, the potential of wrinkle structures in laminar membranes for controllable fluid transport and ion selection needs further study.[26] The analysis in this paper has shown that reversible snap-through of an arched channel makes velocity-controlled ion filtration possible. In this section, we report MD simulations to demonstrate the selection of ions/molecules in the partially fixed arched graphene nanochannel with reversible snap-through. As shown in Figure 5a, Na^+ or Ca^{2+} ions, which are chosen as simple examples, are added into the arched channel with fluid flow, where the size of the channel is related to the selectivity and is characterized by the channel width, d, more directly, the effective channel width, d_0, and the effective narrowest spacing at the arch before and after snap-through, d_1 and d_2, respectively. Here, we consider the channel with d = 1.65 nm (d_0 = 1.31 nm) and arch with w = 4.57 nm, H_0 = 0.667, b = 0.9 nm, accordingly to obtain d_1 = 0.43 nm and d_2 = 0.96 nm. It should be pointed out that the flexible part of the arch deforms during the flow, and the effective narrowest spacings d_1 and d_2 are changed accordingly. As we know that the size of Na^+ is about 0.43 nm,[43] which is roughly equal to d_1, it could pass the arched channel in either the snapped or slightly deformed configurations under flow (see Movie S2). Ca^{2+} ions, with a typical size of 0.54 nm,[43] which is larger than d_1 but smaller than d_2, are blocked by the unsnapped arch as the flow velocity v = 12.6 m/s is smaller than the critical snapping velocity (see Movie S3) but pass through the snapped arch by increasing the flow velocity to above the critical velocity, i.e., v = 88.8 m/s (see Movie S4). According to this fundamental example, we can expect that this type of partially fixed arched graphene nanochannel with reversible snap-through could be employed for the selection of ions with a wide range of sizes by combining the control of the flow velocity.

We also present a phase diagram to demonstrate the selectivity of the arched graphene nanochannels with reversible snap-through for different molecules and ions in Figure 5b: we list 11 ions and molecules with different sizes (all the data are taken from the literature[43]) in the parameter space of the channel width, d, and ion/molecule size. Here, the dimensions of the arch are fixed as w = 4.57 nm, H_0 = 0.667, and b = 0.9 nm. It is clearly seen that the whole space is divided into four phases by the characteristic sizes of the arched channel, d_1, d_2, and d_0. As we mentioned before, the effective narrowest spacing d_1 and d_2 can be changed as the flow in the channel deforms the flexible part of the arch. This increases the uncertainty of phase boundaries (see the shadow areas in Figure 5b). For a channel with a given width d, the ions/molecules with the size in phase (i) can always pass through the channel in the flow with any velocity because their size is smaller than d_1. However, if the size of the ions/molecules locates in phase (ii), they can only pass the channel when the flexible part of the arch is snapped since their sizes fall in between d_1 and d_2; otherwise, they are blocked by the unsnapped arch. The ions/molecules with the size in the phase (iii) are blocked in any case because their size is always larger than d_2. Here, we also mark out the inaccessible phase (iv), where the size is larger than d_0, and the ions/molecules cannot enter the channel.

The phase diagram in Figure 5b clearly shows the function and scope of applications of the arched channel in ion/molecule selection. For given ions/molecules, as we know their size distributions, we can choose an appropriate flow velocity in the channel to control the state of the flexible part of the arch to be snapped or unsnapped and therefore to determine whether specific ions/molecules can pass through. Furthermore, it should be noted that the boundaries between these four phases can be tuned by changing the dimensions of the arch (including span w, amplitude H_0, and fixed length b). Another main advantage of this kind of device is its reusability. The nanochannel with the unsnapped arch performs the selection function (i.e., passing through the small molecules/ions but blocking the large ones), and in the process of selection, large molecules/ions might be concentrated near the arch and block the entire channel eventually. At this point, we can increase the flow rate to activate snap-through of the arch, and therefore allow the blocked molecules/ions to flow out. Then, on slowing down the flow, the arch snaps back and the selection function of the channel is restored accordingly. Reversible snap-through of the partially fixed arch plays a key role in the reusability of this device. In addition, from the perspective of device design, the size of the filtration nanochannel could also be tailored according to the specific ions/molecules to be selected or separated. It is also worth mentioning that the selective transport of ions through nanochannels is a complex process and can be affected by several factors in addition to the size effect.[34,44−46] For example, dehydration of hydrated ions plays an important role in the selection mechanism, owing to the ion-dependent free-energy barriers.[45,46] For the sub-nanometer nanochannel, the dehydration effect is enhanced for hydrated ions with increasing flow velocity. Though the free-energy barriers are typically large and related to the size of the hydration ions, the dehydration level coupling with the channel size and flow velocity needs further study.

CONCLUSIONS

To summarize, we explore the fluid flow in a laminated graphene membrane with wrinkles by simplifying it as a nanochannel embedded with a flexible arch structure. MD simulations were performed, showing that the arched graphene wall can snap from one stable state to another when the fluid flows through the channel reaching a critical velocity, which nonlinearly depends on the geometric sizes of both the channel and the arch and can be predicted by a theoretical model. The flow-induced snap-through of the arch is found to be able to change the channel size and therefore to control the flow behavior, e.g., fluid pressure and hydraulic conductivity within the channel. We further modify the graphene nanochannel by partially fixing the edges of the arch to achieve reversible snap-through. Finally, we demonstrate the potential application of this reversible arched channel for ion/molecule selection. These understandings not only lay the groundwork for understanding the fluid flow in nonflat laminated graphene membranes and other membranes with similar layered microstructures but can also be instructive for the future

https://dx.doi.org/10.1021/acsami.0c16468
ACS Appl. Mater. Interfaces 2021, 13, 1158−1168

design of high-performance and reusable nanofluidic devices for filtration and separation applications.

MODELS AND METHODS

Molecular Structures. The graphene nanochannel connected with a water reservoir on the left side is constructed aligning in the y-direction, as shown in Figure 1c. The nanochannel is made of two parallel graphene sheets with a size of 2.1 × 14.3 nm^2, one of which is compressed at both ends to form an inward flexible arch structure embedded in the middle of two rigid bounds, and the other one is fixed to be fully rigid. Interlayer spacing of the nanochannel measured by the distance between two carbon planes is d = 1.65 nm, which falls within the typical range of the interlayer distance of the graphene oxide membrane measured in water vapor or solution.[2,13,47] The water reservoir size is 8.0, 10.1, and 2.1 nm in the x, y, and z-directions, respectively. The different spans of arch $w \in \{0.9, 1.0, 1.2, 1.5\}\cdot w_0$ (w_0 = 4.57 nm) are considered, and the amplitude of arch h_0 varies from 0.26 to 0.97 nm. The graphene nanochannel and the water reservoir are filled with water with a molecular number N_W = 7430. An open boundary is used in the x-direction, and periodic boundary conditions (PBCs) are applied in the in-plane y and z-directions.

Molecule Dynamics Simulations. MD simulations are performed by employing the large-scale atomic/molecular massively parallel simulator (LAMMPS).[48] The all-atom optimized potentials for liquid simulations (OPLS-AA)[49] are used for graphene sheets. The extended simple point charge (SPC/E) model[50] of water is used in our study, which is widely adopted for MD simulations of water transport as it predicts reasonable density, diffusivity, and viscosity compared to other models.[50−54] Long-range Coulomb interactions are computed using the particle−particle particle−mesh (PPPM) algorithm.[55] The interaction between carbon atoms in graphene and oxygen atoms in water is modeled by parameters ε_{C-O} = 4.063 meV and σ_{C-O} = 0.319 nm, which predict a water contact angle (WCA) of θ = 98.4° for graphene, in consistency with the value measured experimentally.[56,57] The time step to integrate the equation of motion is 1 fs, with the SHAKE algorithm applied for the stretching terms between oxygen and hydrogen atoms of water to avoid the very short integration time step needed for hydrogen-atom-related high-frequency vibrations. Product simulations are carried out after about 1 ns equilibration at 300 K using the Berendsen thermostat with a damping time constant of 100 fs. Key parameters used in our model are listed in Tables S1−S4.[2,18,58] It worth noting that the van der Waals interaction between graphene layers (i.e., the flexible arch and the channel wall on the other side), as well as the interfacial interaction between water and the arch/wall, could be intrinsically captured by the atomic interaction potential in the MD simulation. However, both the mechanical interaction (C−C) and the interfacial interaction (C−O) in the real system are complex, e.g., the existence of water molecules between the graphene layers may affect the effective range of the van der Waals interaction.[59] Therefore, both the mechanical and interfacial interactions are simplified in the simulation, owing to the limitation of the potential function.

Theoretical Model Analysis. It is clearly seen from the MD simulation that the evolution of the shape of the arch and the fluid pressure are coupled during the flow process in the bistable graphene nanochannel. To model the flow−deformation coupling behavior, we simplify the simulation system (i.e., Figure 1c) as a 2D physical model, as shown in Figure 2b, in which the flexible arch can snap from the original state (the upper yellow curve) to the inverted state (the lower blue curve) under the pressure load during the fluid flow process. For the convenience of the analysis, we introduce the flux q_{in} as the characteristic parameter of the channel flow, which can be converted into flow velocity by considering the geometric dimensions of the channel.

Following the previous study proposed by Gomez et al.,[31] the shape of the arch can be described by the linear beam theory, i.e., the transverse displacement, $h(x)$, of the arch satisfies the following one-dimensional beam equation

$$B\frac{d^4h}{dx^4} + T\frac{d^2h}{dx^2} + p(x) = 0,\ 0 < x < w \tag{1}$$

where $B = Et^3/12$ (with Young's modulus, E, and beam thickness, t) is the bending stiffness, T is the unknown compressive force applied to the ends of the arch, and $p(x)$ is the hydrodynamic pressure.

Here, we only consider arch shapes that are well past the Euler-buckling threshold. By neglecting the extensibility, the constraint induced by the imposed end-shortening Δl is

$$\int_0^w \left(\frac{dh}{dx}\right)^2 dx = 2\Delta l \tag{2}$$

The clamped boundaries of the arch at both ends can be expressed as $h(0) = h'(0) = h(w) = h'(w) = 0$; here $()'$ denotes differentiation with respect to x.

To make the beam eq 1 solvable, we need to determine the pressure within the liquid, $p(x)$. Assuming that the reduced Reynolds number (which measures the ratio of inertia to viscosity in the channel with slender geometry) is small and neglecting both the slip effect and the subcontinuum behavior of water flow in the graphene channel, we can employ the lubrication theory[60] to model the thin-film flow in the channel.

According to the lubrication approximation, the pressure gradient, dp/dx, is related to the flux, q_{in}, following Poiseuille's law. Note that here we consider the flow in a 2D channel (since we consider the periodic boundary condition along depth in the z direction) with effective width, d_0, i.e., $q_{in} = q/e$ is the 2D flux with a unit of m^2/s, and, therefore, the horizontal velocity in the channel next to the arch can be calculated as $v = q_{in}/d_0$. Across the length of the arch, the width of the channel varies with position ($0 < x < w$) as $[d_0 - h(x)]$, and we can have the following relation

$$-\frac{[d_0 - h(x)]^3}{12\eta}\frac{dp}{dx} = q_{in},\ 0 < x < w \tag{3}$$

where η is the viscosity coefficient of water. Further downstream, the channel is uniform (with width d_0), and then we have

$$-\frac{d_0^3}{12\eta}\frac{dp}{dx} = q_{in},\ x > w \tag{4}$$

Assuming that the exit end of the channel (i.e., $x = w + w_d$, see Figure 2b) remains at ambient pressure, the fluid pressure $p(x)$ can be obtained by integrating eqs 3 and 4 as

$$p(x) = p(w) + 12\eta q_{in}\int_0^w \frac{1}{[d_0 - h(\zeta)]^3}\,d\zeta,\ 0 < x < w \tag{5}$$

where $p(w) = 12\eta q_{in} w_d/d_0^3$ is the pressure at the downstream end of the arch (relative to the ambient pressure).

The above eqs 1, 2, and 5 provide a closed system to describe the coupling behavior between the arch deformation and the fluid flow. To simplify the calculation, we introduce the dimensionless variables $X = x/w$, $H_0 = h_0/d_0$, and $P = p/p^*$, where $p^* = Bd_0/w^4$ is the natural pressure scale introduced by the beam eq 1. With this non-dimensionalization, we can therefore obtain two key governing parameters: the dimensionless fluid flux $Q = (\eta w^5/Bd_0^4)\cdot q_{in}$ and the dimensionless channel blocking parameter $H_0 = h_0/d_0$.

The analysis by Gomez et al.[31] has shown that snap-through transition is a saddle-node bifurcation, i.e., a constricting state ceases to exist at a critical value $Q = Q_{snap}$ without first becoming unstable. Therefore, we can numerically calculate the Q_{snap} as a function of H_0 by solving the dimensionless versions of eqs 1, 2, and 5. Furthermore, the critical nondimensional flux at snap-through transition Q_{snap} can be related to the critical velocity v_{snap} through the following relation

$$v_{snap} = \varepsilon\cdot(Bd_0^3/\eta w^5)\cdot Q_{snap} \tag{6}$$

where ε is the enhancement factor induced by the slip effect, which can be obtained through the simulation, and here we find its value with the order of about 20. According to eq 6, the critical velocities

https://dx.doi.org/10.1021/acsami.0c16468
ACS Appl. Mater. Interfaces 2021, 13, 1158−1168

v_{snap} for different cases with different w values can be scaled into the dimensionless critical flux Q_{snap}. Taking the case of $w = w_0 = 4.57$ nm as an example, by introducing the related parameters in eq 6, $B = 1.25$ eV, $\eta = 0.8$ mPa·s, and $d_0 = 1.31$ nm, the prefactor $\alpha = Bd_0^3/\eta w^5$ can be calculated as $\alpha = 0.2834$. The critical velocity can be obtained as $Q_{snap} = v_{snap}/(\varepsilon\cdot\alpha) = 0.1764v_{snap}$. It should also be noted that, according to the previous study,[22] the enhancement factor with respect to the case of the no-slip boundary condition for a uniform channel can be estimated by $\varepsilon = 1 + 6L_s/d_0$, where L_s and d_0 are the slip length and the channel size, respectively. Specific to our analysis here, considering $L_s \approx 50$ nm according to the previously reported data,[22] the predicted enhancement factor of the whole channel is about 230, which is much larger than the calculated value from the simulation of the arched channel. This indicated that the enhancement effect in this kind of flexible nonuniform channel is more complex and cannot be predicted by the simple reported correlation. We leave a detailed analysis of the relation between the enhancement factor and the geometric parameters of the flexible nonuniform channel for a future study.

■ ASSOCIATED CONTENT

Supporting Information

The Supporting Information is available free of charge at https://pubs.acs.org/doi/10.1021/acsami.0c16468.

Additional data and figures including parameters of the atomic potential function and the relationship between the number of water molecules exiting the outlet and time (PDF)

Snap-through of the flexible arch in the graphene nanochannel under fluid flow (MP4)

Passage of Na^+ through the arched nanochannel (MP4)

Blockage of Ca^{2+} through the unsnapped arched nanochannel when the flow velocity is below the critical snapping velocity (MP4)

Passage of Ca^{2+} through the snapped arched nanochannel when the flow velocity is above the critical snapping velocity (MP4)

■ AUTHOR INFORMATION

Corresponding Author

Mingchao Liu − *Mathematical Institute, University of Oxford, Oxford OX2 6GG, U.K.;* orcid.org/0000-0001-7424-4794; Email: Mingchao.Liu@maths.ox.ac.uk

Author

Shuping Jiao − *Shanghai Key Laboratory of Mechanics in Energy Engineering, Shanghai Institute of Applied Mathematics and Mechanics, School of Mechanics and Engineering Science, Shanghai University, Shanghai 200444, China*

Complete contact information is available at: https://pubs.acs.org/10.1021/acsami.0c16468

Author Contributions

M.L. and S.J. designed the study. S.J. performed the simulations. M.L. performed the theoretical analysis. S.J. and M.L. analyzed the data and wrote the manuscript.

Notes

The authors declare no competing financial interest.

■ ACKNOWLEDGMENTS

We thank D. Vella, M. Gomez, and Z. Dai for many rounds of discussion, invaluable comments, and their critical reading of this manuscript. S.J. acknowledges the support by the National Natural Science Foundation of China under Grant no. 11902186. M.L. acknowledges the support from the Newton International Fellowship founded by the Royal Society (NIF \R1\180165).

■ REFERENCES

(1) Chen, L.; Shi, G.; Shen, J.; Peng, B.; Zhang, B.; Wang, Y.; Bian, F.; Wang, J.; Li, D.; Qian, Z.; Xu, G.; Liu, G.; Zeng, J.; Zhang, L.; Yang, Y.; Zhou, G.; Wu, M.; Jin, W.; Li, J.; Fang, H. Ion Sieving in Graphene Oxide Membranes via Cationic Control of Interlayer Spacing. *Nature* **2017**, *550*, 380−383.

(2) Abraham, J.; Vasu, K. S.; Williams, C. D.; Gopinadhan, K.; Su, Y.; Cherian, C. T.; Dix, J.; Prestat, E.; Haigh, S. J.; Grigorieva, I. V.; Carbone, P.; Geim, A. K.; Nair, R. R. Tunable Sieving of Ions Using Graphene Oxide Membranes. *Nat. Nanotechnol.* **2017**, *12*, 546−550.

(3) Radha, B.; Esfandiar, A.; Wang, F. C.; Rooney, A. P.; Gopinadhan, K.; Keerthi, A.; Mishchenko, A.; Janardanan, A.; Blake, P.; Fumagalli, L.; Lozada-Hidalgo, M.; Garaj, S.; Haigh, S. J.; Grigorieva, I. V.; Wu, H. A.; Geim, A. K. Molecular Transport through Capillaries Made with Atomic-scale Precision. *Nature* **2016**, *538*, 222−225.

(4) Esfandiar, A.; Radha, B.; Wang, F. C.; Yang, Q.; Hu, S.; Garaj, S.; Nair, R. R.; Geim, A. K.; Gopinadhan, K. Size Effect in Ion Transport through Angstrom-scale Slits. *Science* **2017**, *358*, 511−513.

(5) Kim, H. W.; Yoon, H. W.; Yoon, S. M.; Yoo, B. M.; Ahn, B. K.; Cho, Y. H.; Shin, H. J.; Yang, H.; Paik, U.; Kwon, S.; Choi, J. Y.; Park, H. B. Selective Gas Transport through Few-layered Graphene and Graphene Oxide Membranes. *Science* **2013**, *342*, 91−95.

(6) Li, H.; Song, Z.; Zhang, X.; Huang, Y.; Li, S.; Mao, Y.; Ploehn, H. J.; Bao, Y.; Yu, M. Ultrathin, Molecular-Sieving Graphene Oxide Membranes for Selective Hydrogen Separation. *Science* **2013**, *342*, 95−98.

(7) Joshi, R.; Carbone, P.; Wang, F. C.; Kravets, V. G.; Su, Y.; Grigorieva, I. V.; Wu, H.; Geim, A. K.; Nair, R. R. Precise and Ultrafast Molecular Sieving through Graphene Oxide Membranes. *Science* **2014**, *343*, 752−754.

(8) Mi, B. Graphene Oxide Membranes for Ionic and Molecular Sieving. *Science* **2014**, *343*, 740−742.

(9) Yumura, T.; Yamasaki, A. Roles of Water Molecules in Trapping Carbon Dioxide Molecules inside the Interlayer Space of Graphene Oxides. *Phys. Chem. Chem. Phys.* **2014**, *16*, 9656−9666.

(10) Olson, E. J.; Ma, R.; Sun, T.; Ebrish, M. A.; Haratipour, N.; Min, K.; Aluru, N. R.; Koester, S. J. Capacitive Sensing of Intercalated H_2O Molecules Using Graphene. *ACS Appl. Mater. Interfaces* **2015**, *7*, 25804−25812.

(11) Tong, W. L.; Ong, W. J.; Chai, S. P.; Tan, M. K.; Huang, Y. M. Enhanced Evaporation Strength through Fast Water Permeation in Graphene-Oxide Deposition. *Sci. Rep.* **2015**, *5*, No. 11896.

(12) Nair, R. R.; Wu, H. A.; Jayaram, P. N.; Grigorieva, I. V.; Geim, A. K. Unimpeded Permeation of Water through Helium-leak-tight Graphene-based Membranes. *Science* **2012**, *335*, 442−444.

(13) Zheng, S.; Tu, Q.; Wang, M.; Urban, J. J.; Mi, B. Correlating Interlayer Spacing and Separation Capability of Graphene Oxide Membranes in Organic Solvents. *ACS Nano* **2020**, *14*, 6013−6023.

(14) Lerf, A.; Buchsteiner, A.; Pieper, J.; Schöttl, S.; Dekany, I.; Szabo, T.; Boehm, H. P. Hydration Behavior and Dynamics of Water Molecules in Graphite Oxide. *J. Phys. Chem. Solids* **2006**, *67*, 1106−1110.

(15) Secchi, E.; Marbach, S.; Nigues, A.; Stein, D.; Siria, A.; Bocquet, L. Massive Radius-dependent Flow Slippage in Carbon Nanotubes. *Nature* **2016**, *537*, 210−213.

(16) Tunuguntla, R. H.; Henley, R. Y.; Yao, Y. C.; Pham, T. A.; Wanunu, M.; Noy, A. Enhanced Water Permeability and Tunable Ion Selectivity in Subnanometer Carbon Nanotube Porins. *Science* **2017**, *357*, 792−796.

(17) Marcotte, A.; Mouterde, T.; Nigues, A.; Siria, A.; Bocquet, L. Mechanically Activated Ionic Transport across Single-digit Carbon Nanotubes. *Nat. Mater.* **2020**, *19*, 1057−1061.

(18) Wei, N.; Peng, X.; Xu, Z. Breakdown of Fast Water Transport in Graphene Oxides. *Phys. Rev. E* **2014**, *89*, No. 012113.
(19) Saraswat, V.; Jacobberger, R. M.; Ostrander, J. S.; Hummell, C. L.; Way, A. J.; Wang, J.; Zanni, M. T.; Arnold, M. S. Invariance of Water Permeance through Size-differentiated Graphene Oxide Laminates. *ACS Nano* **2018**, *12*, 7855−7865.
(20) Dave, S. H.; Gong, C.; Robertson, A. W.; Warner, J. H.; Grossman, J. C. Chemistry and Structure of Graphene Oxide via Direct Imaging. *ACS Nano* **2016**, *10*, 7515−7522.
(21) Yang, Q.; Su, Y.; Chi, C.; Cherian, C. T.; Huang, K.; Kravets, V. G.; Wang, F. C.; Zhang, J. C.; Pratt, A.; Grigorenko, A. N.; Guinea, F.; Geim, A. K.; Nair, R. R. Ultrathin Graphene-based Membrane with Precise Molecular Sieving and Ultrafast Solvent Permeation. *Nat. Mater.* **2017**, *16*, 1198−1202.
(22) Wei, N.; Peng, X.; Xu, Z. Understanding Water Permeation in Graphene Oxide Membranes. *ACS Appl. Mater. Interfaces* **2014**, *6*, 5877−5883.
(23) Algara-Siller, G.; Lehtinen, O.; Wang, F. C.; Nair, R. R.; Kaiser, U.; Wu, H. A.; Geim, A. K.; Grigorieva, I. V. Square Ice in Graphene Nanocapillaries. *Nature* **2015**, *519*, 443−445.
(24) Chen, J.; Schusteritsch, G.; Pickard, C. J.; Salzmann, C. G.; Michaelides, A. Two Dimensional Ice from First Principles: Structures and Phase Transitions. *Phys. Rev. Lett.* **2016**, *116*, No. 025501.
(25) Jiao, S.; Xu, Z. Non-continuum Intercalated Water Diffusion Explains Fast Permeation through Graphene Oxide Membranes. *ACS Nano* **2017**, *11*, 11152−11161.
(26) Kang, Y.; Qiu, R.; Jian, M.; Wang, P.; Xia, Y.; Motevalli, B.; Zhao, W.; Tian, Z.; Liu, J. Z.; Wang, H.; Liu, H.; Zhang, X. The Role of Nanowrinkles in Mass Transport across Graphene-based Membranes. *Adv. Funct. Mater.* **2020**, *30*, No. 2003159.
(27) Jiao, S.; Xu, Z. Selective Gas Diffusion in Graphene Oxides Membranes: A Molecular Dynamics Simulations Study. *ACS Appl. Mater. Interfaces* **2015**, *7*, 9052−9059.
(28) Jiao, S.; Zhou, K.; Wu, M.; Li, C.; Cao, X.; Zhang, L.; Xu, Z. Confined Structures and Selective Mass Transport of Organic Liquids in Graphene Nanochannels. *ACS Appl. Mater. Interfaces* **2018**, *10*, 37014−37022.
(29) Deng, S.; Berry, V. Wrinkled, Rippled and Crumpled Graphene: An Overview of Formation Mechanism, Electronic Properties, and Applications. *Mater. Today* **2016**, *19*, 197−212.
(30) Holmes, D. P.; Tavakol, B.; Froehlicher, G.; Stone, H. A. Control and Manipulation of Microfluidic Flow via Elastic Deformations. *Soft Matter* **2013**, *9*, 7049−7053.
(31) Gomez, M.; Moulton, D. E.; Vella, D. Passive Control of Viscous Flow via Elastic Snap-through. *Phys. Rev. Lett.* **2017**, *119*, No. 144502.
(32) Arena, G.; Groh, R. M. J.; Theunissen, R.; Weaver, P. M.; Pirrera, A. Design and Testing of a Passively Adaptive Inlet. *Smart Mater. Struct.* **2018**, *27*, No. 085019.
(33) Arena, G.; Groh, R. M. J.; Brinkmeyer, A.; Theunissen, R.; Weaver, P. M.; Pirrera, A. Adaptive Compliant Structures for Flow Regulation. *Proc. R. Soc. A* **2017**, *473*, No. 20170334.
(34) Zhou, K.; Xu, Z. Renormalization of Ionic Solvation Shells in Nanochannels. *ACS Appl. Mater. Interfaces* **2018**, *10*, 27801−27809.
(35) Pandey, A.; Moulton, D. E.; Vella, D.; Holmes, D. P. Dynamics of Snapping Beams and Jumping Poppers. *Europhys. Lett.* **2014**, *105*, No. 24001.
(36) Lu, Q.; Arroyo, M.; Huang, R. Elastic Bending Modulus of Monolayer Graphene. *J. Phys. D: Appl. Phys.* **2009**, *42*, No. 102002.
(37) Ahmadpoor, F.; Wang, P.; Huang, R.; Sharma, P. Thermal Fluctuations and Effective Bending Stiffness of Elastic Thin Sheets and Graphene: A Nonlinear Analysis. *J. Mech. Phys. Solids* **2017**, *107*, 294−319.
(38) Thomas, J. A.; McGaughey, A. J. Water Flow in Carbon Nanotubes: Transition to Subcontinuum Transport. *Phys. Rev. Lett.* **2009**, *102*, No. 184502.
(39) Kannam, S. K.; Todd, B. D.; Hansen, J. S.; Daivis, P. J. Slip Length of Water on Graphene: Limitations of Non-equilibrium Molecular Dynamics Simulations. *J. Chem. Phys.* **2012**, *136*, No. 024705.
(40) Xie, Q.; Alibakhshi, M. A.; Jiao, S.; Xu, Z.; Hempel, M.; Kong, J.; Park, H. G.; Duan, C. Fast Water Transport in Graphene Nanofluidic Channels. *Nat. Nanotechnol.* **2018**, *13*, 238−245.
(41) Gopinadhan, K.; Hu, S.; Esfandiar, A.; Lozada-Hidalgo, M.; Wang, F. C.; Yang, Q.; Tyurnina, A. V.; Keerthi, A.; Radha, B.; Geim, A. K. Complete Steric Exclusion of Ions and Proton Transport through Confined Monolayer Water. *Science* **2019**, *363*, 145−148.
(42) Bocquet, L. Nanofluidics Coming of Age. *Nat. Mater.* **2020**, *19*, 254−256.
(43) Marcus, Y. A Simple Empirical Model Describing the Thermodynamics of Hydration of Ions of Widely Varying Charges, Sizes, and Shapes. *Biophys. Chem.* **1994**, *51*, 111−127.
(44) Eisenman, G.; Horn, R. Ionic Selectivity Revisited: The Role of Kinetic and Equilibrium Processes in Ion Permeation through Channels. *J. Membr. Biol.* **1983**, *76*, 197−225.
(45) Sahu, S.; Di Ventra, M.; Zwolak, M. Dehydration as a Universal Mechanism for Ion Selectivity in Graphene and Other Atomically Thin Pores. *Nano Lett.* **2017**, *17*, 4719−4724.
(46) Li, Z.; Li, Y.; Yao, Y. C.; Aydin, F.; Zhan, C.; Chen, Y.; Elimelech, M.; Pham, T. A.; Noy, A. Strong Differential Monovalent Anion Selectivity in Narrow Diameter Carbon Nanotube Porins. *ACS Nano* **2020**, *14*, 6269−6275.
(47) Zheng, S.; Tu, Q.; Urban, J. J.; Li, S.; Mi, B. Swelling of Graphene Oxide Membranes in Aqueous Solution: Characterization of Interlayer Spacing and Insight into Water Transport Mechanisms. *ACS Nano* **2017**, *11*, 6440−6450.
(48) Plimpton, S. Fast Parallel Algorithms for Short-range Molecular Dynamics. *J. Comput. Phys.* **1995**, *117*, 1−19.
(49) Jorgensen, W. L.; Maxwell, D. S.; Tirado-Rives, J. Development and Testing of the OPLS All-Atom Force Field on Conformational Energetics and Properties of Organic Liquids. *J. Am. Chem. Soc.* **1996**, *118*, 11225−11236.
(50) Berendsen, H. J. C.; Grigera, J. R.; Straatsman, T. P. The Missing Term in Effective Pair Potentials. *J. Phys. Chem. A* **1987**, *91*, 6269−6271.
(51) Svishchev, I. M.; Kusalik, P. G.; Wang, J.; Boyd, R. J. Polarizable Point-charge Model for Water: Results under Normal and Extreme Conditions. *J. Chem. Phys.* **1996**, *105*, 4742−4750.
(52) Báez, L. A.; Clancy, P. Existence of A Density Maximum in Extended Simple Point Charge Water. *J. Chem. Phys.* **1994**, *101*, 9837−9840.
(53) Wu, Y.; Tepper, H. L.; Voth, G. A. Flexible Simple Point-charge Water Model with Improved Liquid-state Properties. *J. Chem. Phys.* **2006**, *124*, No. 024503.
(54) Giovambattista, N.; Rossky, P. J.; Debenedetti, P. G. Phase Transitions Induced by Nanoconfinement in Liquid Water. *Phys. Rev. Lett.* **2009**, *102*, No. 050603.
(55) Hockney, R. W.; Eastwood, J. W. *Computer Simulation Using Particles.*; Taylor & Francis, 1989.
(56) Rafiee, J.; Mi, X.; Gullapalli, H.; Thomas, A. V.; Yavari, F.; Shi, Y.; Ajayan, P. M.; Koratkar, N. A. Wetting Transparency of Graphene. *Nat. Mater.* **2012**, *11*, 217−222.
(57) Wei, N.; Peng, X.; Xu, Z. Breakdown of Fast Water Transport in Graphene Oxides. *Phys. Rev. E* **2014**, *89*, No. 012113.
(58) Shih, C. J.; Lin, S.; Sharma, R.; Strano, M. S.; Blankschtein, D. Understanding the pH-Dependent Behavior of Graphene Oxide Aqueous Solutions: A Comparative Experimental and Molecular Dynamics Simulation Study. *Langmuir* **2012**, *28*, 235−241.
(59) Dai, Z.; Lu, N.; Liechti, K. M.; Huang, R. Mechanics at the Interfaces of 2D Materials: Challenges and Opportunities. *Curr. Opin. Solid State Mater. Sci.* **2020**, *24*, No. 100837.
(60) Ockendon, H.; Ockendon, J. R. *Viscous Flow*; Cambridge University Press: Cambridge, 1995.

https://dx.doi.org/10.1021/acsami.0c16468
ACS Appl. Mater. Interfaces 2021, 13, 1158−1168